Optimizing Interface Conductivity in Electronics

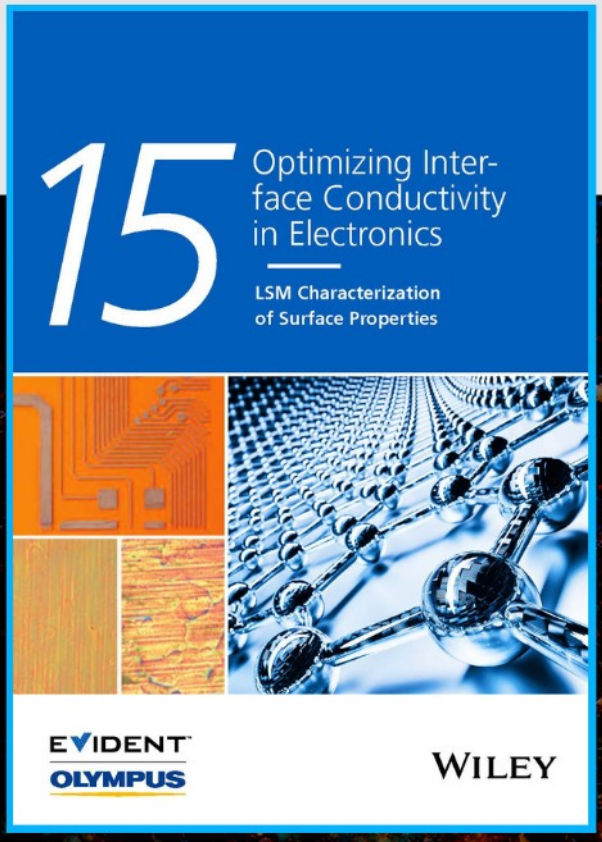

The latest eBook from Advanced Optical Metrology. Download for free.

Surface roughness is a key parameter for judging the performance of a given material's surface quality for its electronic application. A powerful tool to measure surface roughness is 3D laser scanning confocal microscopy (LSM), which will allow you to assess roughness and compare production and finishing methods, and improve these methods based on mathematical models.

Focus on creating high-conductivity electronic devices with minimal power loss using laser scanning microscopy is an effective tool to discern a variety of roughness parameters.

EVIDENT
OLYMPUS

WILEY

ADVANCED FUNCTIONAL MATERIALS
www.afm-journal.de

Manipulating Spin Exchange Interactions and Spin-Selected Electron Transfers of 2D Metal Phosphorus Trisulfide Crystals for Efficient Oxygen Evolution Reaction

Chih-Ying Huang, Hung-Min Lin, Chun-Hao Chiang, Hsin-An Chen, Ting-Ran Liu, Deepak Vishnu S. K, Jau-Wern Chiou, Raman Sankar,* Huang-Ming Tsai, Way-Faung Pong,* and Chun-Wei Chen**

Because oxygen molecules in the ground state favor a triplet spin configuration, spin-polarized electrons at electrocatalysts may promote the generation of parallel spin-aligned oxygen atoms, enhancing oxygen evolution reaction (OER) kinetics. In this study, a significant enhancement of OER performance is demonstrated by controlling the spin-exchange interaction and spin-selected electron transfer of 2D $Co_xFe_{1-x}PS_3$ ($x = 0$–0.45) van der Waals (vdW) single crystals through Co doping. The pristine $FePS_3$ exhibits antiferromagnetic orbital ordering, while the Co-doped $FePS_3$ exhibits the emergence of interatomic ferromagnetism due to doping-mediated magnetic exchange interactions. The coupling between Fe and Co ions in the Co-doped $FePS_3$ crystal allows the formation of efficient spin-selective electron transfer channels compared to the pristine $FePS_3$. The correlation of spin-exchange interactions and spin-selected electron transfers of 2D Co-doped $FePS_3$ crystals with a superior OER performance is further revealed by superconducting quantum interference device magnetometer, in situ X-ray absorption near edge spectra and density functional theory simulations. The result suggests that manipulating the spin-exchange interactions of 2D vdW crystals to enhance the spin-selected electron transfer efficiencies through doping is an effective strategy to boost their OER catalytic performances.

1. Introduction

The need for sustainable energy resources has become increasingly apparent as modern society develops. Fossil fuel reserves are dwindling, and the consequences of climate change are becoming more severe.[1] Researchers are exploring more efficient, clean, and sustainable alternatives. One such alternative is hydrogen (H_2), which has gained significant attention recently due to its potential for the worldwide development of clean energy, zero carbon emissions, and high combustion heat value.[2] One environmentally-friendly method for H_2 production is the water-splitting process, which can be achieved through various techniques, including photochemical, electrochemical, and photoelectrochemical methods.[3] Among these techniques, electrochemical water splitting has emerged as a preferred approach to scale up the high purity of H_2 production and achieve energetic sustainability.[4] However, the high

C.-Y. Huang, C.-W. Chen
International Graduate Program of Molecular Science and Technology (NTU-MST)
National Taiwan University
Taipei 106319, Taiwan
E-mail: d09551003@ntu.edu.tw

C.-Y. Huang, D. Vishnu S. K
Molecular Science and Technology Program
Taiwan International Graduate Program (TIGP)
Academia Sinica
Taipei 115201, Taiwan

H.-M. Lin, C.-H. Chiang, T.-R. Liu, C.-W. Chen
Department of Materials Science and Engineering
National Taiwan University
Taipei 106319, Taiwan

The ORCID identification number(s) for the author(s) of this article can be found under https://doi.org/10.1002/adfm.202305792

DOI: 10.1002/adfm.202305792

H.-A. Chen
Institute of Materials Science and Engineering
National Taipei University of Technology
Taipei 10608, Taiwan
E-mail: hachen@mail.ntut.edu.tw

D. Vishnu S. K
Department of Chemistry
National Tsing Hua University
Hsinchu 300044, Taiwan

J.-W. Chiou
Department of Applied Physics
National University of Kaohsiung
Kaohsiung 811726, Taiwan
E-mail: jwchiou@nuk.edu.tw

R. Sankar
Institute of Physics
Academia Sinica
Taipei 115201, Taiwan
E-mail: sankarraman@gate.sinica.edu.tw

activation barriers and sluggish kinetics of the anodic oxygen evolution reaction (OER) severely hinder the overall efficiency of water electrolysis, making it a bottleneck for large-scale industrial applications.[3b,5] To address this challenge, there is a pressing need to develop low-cost, efficient, and stable electrocatalysts for the OER.

The understanding of OER mechanisms is critical for the development of highly active and stable electrocatalysts. Various fundamental mechanisms have been proposed to guide the design of efficient OER catalysts. One widely studied mechanism is the electron transfer steps involved in the adsorption and desorption of intermediates on the active sites.[6] The e_g theory explains the correlation between the binding energy of transition metals and surface oxygen with the active transition metal ion's e_g value, specifically for perovskite OER catalysts.[7] However, some exceptions have been found not well fitted with the e_g theory, partially due to the diverse and complicated magnetism in the transition metal oxides family. The ground state of di-oxygen is a spin triplet with the lowest energy, while the excited state of di-oxygen and the reactants (H_2O and OH^-) are a spin singlet with about 1 eV higher. Therefore, the spin between the reactants or products in the OER reaction is not conserved and requires extra energy to drive.[8] Recent theoretical studies have proposed using quantum spin-exchange interactions (QSEI) to explain the enhanced catalytic activity of OER by manipulating the spin configuration of catalysts.[9] The spin-polarized electrons on the active catalyst surface promote the generation of parallel spin-aligned oxygens, which further improve the performance of OER.[10] Accordingly, reaction kinetics (thus catalytic activity) generally increase when interatomic ferromagnetic (FM) interactions are dominant, while it sensibly decreases when antiferromagnetic (AFM) interactions prevail.[11] The effect of direct magnetic field-enhanced electrocatalytic water oxidation was recently observed, and the enhancement is positively correlated with magnetization.[12] A series of experiments show that efficient spin-related electron transfer by engineering the local spin-states of catalysts is the origin of the enhanced OER process.[13] Therefore, controlling the spin configurations of catalysts plays an important role in designing highly efficient OER catalysts.

2D van der Waals (vdW) materials have attracted great interest due to their novel physical properties in electronics, optics, and spintronics.[14] In particular, the realization of magnetism in the exfoliated 2D vdW crystals provides accessibility to control the magnetic properties at a single atomic layer level.[15] Among them, transition metal phosphorus trichalcogenides are a series of ternary layered materials stacked through weak vdW forces and belong to a monoclinic system with general formula MPX_3 (M = Fe, Co, Ni, and Mn; X = S and Se). Bulk crystals of MPX_3 with a 2D graphene-like honeycomb lattice arrangement have gained attention due to their interesting magnetic and superconductive properties.[16] In addition, MPX_3 materials have been considered promising catalysts for water-splitting reactions due to their band structures with electron affinity and electronegativity that allow both efficient hydrogen evolution reaction (HER) and OER.[17] Many research works have reported the excellent OER performances of MPX_3-based catalysts.[18] For example, $NiPS_3$ nanosheets doped with a certain amount of Fe exhibit excellent HER and OER activities for water splitting.[19] Until now, the fundamental understanding of OER mechanisms of MPX_3-based catalysts mainly focuses on the thermodynamic process of adsorption and desorption between active sites and intermediates.[20] The spin configuration of the oxygen product and its coupling with the electrocatalyst has been ignored. However, the local spin states may play an important role in determining the OER catalytic activities.[21]

In this work, a significant improvement in the corresponding OER performance can be achieved by controlling the spin configurations and exchange interactions of 2D $Co_xFe_{1-x}PS_3$ (x = 0–0.45) vdW single crystals through Co doping. The pristine $FePS_3$ exhibits AFM orbital ordering, while the Co-doped $FePS_3$ exhibits the suppression of AFM orbital orderings and the emergence of weak interatomic ferromagnetism resulting from doping-mediated magnetic exchange interactions. The introduction of Co into $FePS_3$ crystals provides a large number of Co^{2+} high-spin states, which are responsible for the active sites of OER. In addition, the Co-doped $FePS_3$ exhibits more efficient spin-selected electron transfer than the pristine $FePS_3$. Accordingly, $Fe_{0.55}Co_{0.45}PS_3$ crystals exhibit an outstanding OER performance with an onset potential of 290 mV (on Ni foam) and 310 mV (on carbon fiber paper) at a 10 mA cm^{-2} current density of oxygen generation, outperforming the OER performance of the pristine $FePS_3$. The fundamental understanding of the superior OER performance of Co-doped $FePS_3$ compared to the pristine $FePS_3$ is further systematically explored by superconducting quantum interference device (SQUID) magnetometer, in situ X-ray absorption near edge spectra (XANES) and density functional theory (DFT) simulations. Our result suggests that tuning local spin configurations and spin exchange interactions in 2D vdW crystals through doping is an effective strategy to boost their OER efficiencies.

2. Results and Discussions

The high-quality $FePS_3$ and $Co_xFe_{1-x}PS_3$ (x = 0.15, 0.30, 0.45) crystals were grown using a chemical vapor transport (CVT) method. The maximum cobalt doping limit in $FePS_3$ is $x = 0.45$. If cobalt doping exceeds more than 0.45 ($x > 0.45$), the magnetic impurity of Co_2P appears. **Figure 1**a,b shows the top and side view of the crystal structure of $Co_xFe_{1-x}PS_3$, respectively. $Co_xFe_{1-x}PS_3$ is a monoclinic layered material with a space group of $C2/m$, and every single Fe (or Co) coordinates with six sulfur atoms which form a honeycomb structure. The transition metal ions (Co and Fe) honeycomb lattice is distributed around the $(P_2S_6)^{4-}$ bipyramids with a vdW interaction between every two

H.-M. Tsai
National Synchrotron Radiation Research Center
Hsinchu 300092, Taiwan
W.-F. Pong
Department of Physics
Tamkang University
New Taipei City 251301, Taiwan
E-mail: wfpong@gms.tku.edu.tw
C.-W. Chen
Center of Atomic Initiative for New Materials (AI-MAT)
National Taiwan University
Taipei 106319, Taiwan
E-mail: chunwei@ntu.edu.tw

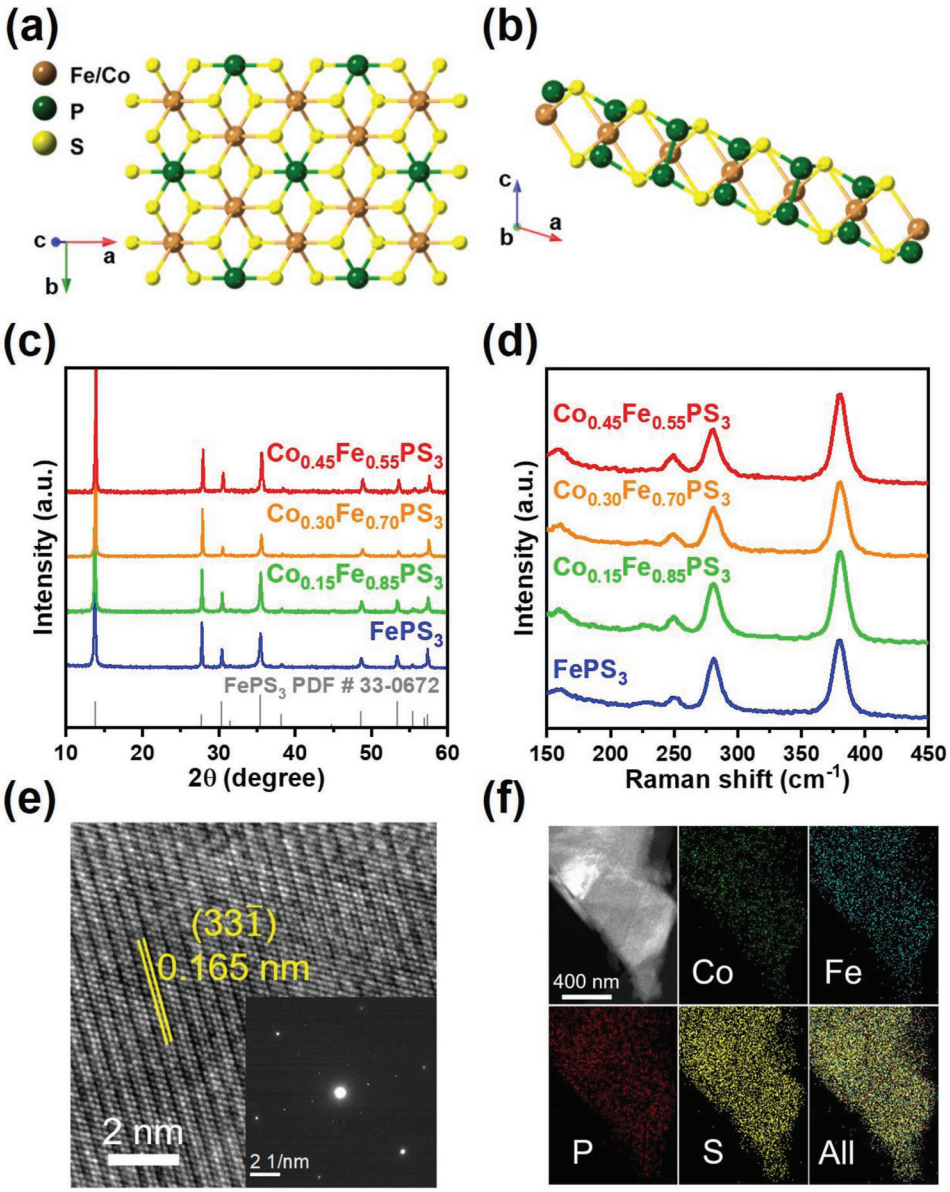

Figure 1. Structure characterization of $Co_xFe_{1-x}PS_3$ ($x = 0$, 0.15, 0.30, 0.45) crystals. a) Crystal structure models of $Co_xFe_{1-x}PS_3$ monolayer along the *c*-axis, and b) *b*-axis. c) Powder XRD patterns of $Co_xFe_{1-x}PS_3$ compare with the standard $FePS_3$ (PDF #33-0672). d) Raman spectra of $Co_xFe_{1-x}PS_3$. e) HRTEM image and SAED pattern of $Co_{0.45}Fe_{0.55}PS_3$ along the [103] zone axis shown in the inset. f) EDS mapping images of $Co_{0.45}Fe_{0.55}PS_3$.

atomic layers along the *c* axis. This layered structure can be exfoliated to a few layers (or a single layer) by the mechanical exfoliation method and the layered crystal image is shown in Figure S1a (Supporting Information). The $FePS_3$ and $Co_xFe_{1-x}PS_3$ ($x = 0.15$, 0.30, 0.45) crystal structure and composition were further verified by the powder X-ray diffraction (XRD), as shown in Figure 1c. The diffraction peaks of all samples fit well with that of the standard $FePS_3$ (PDF#33-0672, a = 5.947° Å, b = 10.3° Å, c = 6.722° Å, $\beta = 107.16°$), and there are no other impurity phases in all samples. The sharp diffraction peaks were observed for the (00*l*) plane, which suggests the good crystallinity and layered structure of the samples. Besides, $Co_xFe_{1-x}PS_3$ has the same monoclinic crystal structure and symmetry as that of $FePS_3$ ($C2/m$). As the content of the Co ion is increased, the main (001) peak slightly shifted to a higher angle (from 13.79° to 13.92°), which is caused by the lattice contraction when the Fe ions are partially substituted by Co ions with a smaller ionic radius.[22] Raman spectra show the intramolecular vibrations from $(P_2S_6)^{4-}$ bipyramid structure peaks at 250 and 380 cm^{-1}, which stand for the out-of-plane A_{1g} modes. Meanwhile, the peak at 280 cm^{-1} represents the in-plane E_g mode (Figure 1d). No other peaks were observed in the Raman spectra for all the samples, which indicated the absence of chemical impurities. Besides, the similar Raman shift denotes that the structure of $Co_xFe_{1-x}PS_3$ remains the same when the Co ions concentration is increased. Transmission electron microscopy (TEM) is used to evaluate the morphological

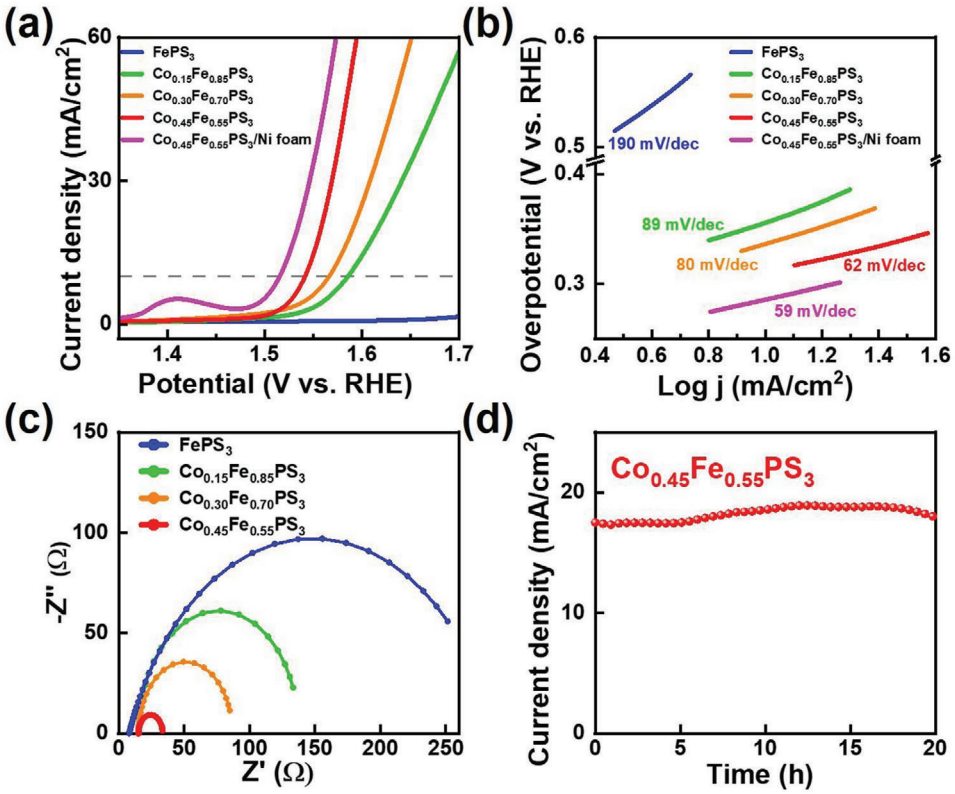

Figure 2. Electrochemical catalytic activity for OER. a) iR-corrected LSV curves recorded in 1 M KOH electrolyte at a scan rate of 10 mV s^{-1}. b) Tafel plots. c) EIS of $Co_xFe_{1-x}PS_3$. d) The 20 h stability test of $Co_{0.45}Fe_{0.55}PS_3$ at a constant potential of 1.55 V versus RHE.

quality, and it reveals the thin and layered nanosheet morphology of the $Co_{0.45}Fe_{0.55}PS_3$ crystal, as shown in Figure S1b (Supporting Information). In addition, a high-resolution TEM (HRTEM) image shows the clear lattice fringe of 0.165 nm, and the corresponding selected area electron diffraction (SAED) pattern is indexed to the monoclinic crystal structure along the (103) axis, further confirming the crystallinity of the $Co_{0.45}Fe_{0.55}PS_3$ crystals (Figure 1e). To get the details about element distribution, dark field image, and energy-dispersive spectroscopy (EDS) mapping were carried out on the $Co_{0.45}Fe_{0.55}PS_3$ crystals in Figure 1f. It reveals a homogenous distribution of Fe, Co, P, and S elements in the $Co_{0.45}Fe_{0.55}PS_3$ crystals.

To investigate the electrocatalytic OER activities of $FePS_3$ and $Co_xFe_{1-x}PS_3$ ($x = 0.15, 0.30, 0.45$) crystals, we adopt the typical three-electrode system which is composed of Ag/AgCl (3 M KCl) as reference electrode, Pt wire as a counter electrode, and carbon fiber paper with our catalysts as a working electrode in 1 M KOH electrolyte. **Figure 2**a shows the linear sweep voltammetry (LSV) curves of $FePS_3$ and $Co_xFe_{1-x}PS_3$ crystals, which shows that the increased cobalt dopant concentration enhances the current density and boosts the overpotential dramatically. The pristine $FePS_3$ exhibits a poor overpotential of 620 mV at 10 mA cm^{-2} for OER. By contrast, the OER performance of $Co_xFe_{1-x}PS_3$ crystals is significantly improved by showing a decreasing overpotential with an increased Co concentration. In particular, $Co_{0.45}Fe_{0.55}PS_3$ shows the best overpotential versus RHE of 310 mV at a current density of 10 mA cm^{-2} on carbon fiber paper. The OER performance of $Co_{0.45}Fe_{0.55}PS_3$ is further improved when loaded on a nickel foam substrate, exhibiting an enhanced overpotential of 290 mV due to the high surface area of an open-porous foam-type substrate. The corresponding Tafel slopes also reveal the improved reaction kinetics of Co-doped $FePS_3$ crystals as shown in Figure 2b. The Tafel slope of $Co_{0.45}Fe_{0.55}PS_3$ is only 62 mV dec^{-1} (59 mV dec^{-1} on Ni-form substrate), which is smaller than that of $Co_{0.30}Fe_{0.70}PS_3$ (80 mV dec^{-1}), $Co_{0.15}Fe_{0.85}PS_3$ (89 mV dec^{-1}), and $FePS_3$ (190 mV dec^{-1}). A smaller Tafel slope means $Co_{0.45}Fe_{0.55}PS_3$ has a most favorable reaction kinetics with a faster reaction rate for accelerating the rapid oxygen production in the OER process. Electrochemical impedance spectroscopy (EIS) was employed to evaluate the charge transfer resistance of the catalyst during OER (Figure 2c). The semicircles in the Nyquist plots were fitted using Randle's equivalent circuit model, which consists of the electrolyte and electrolyte-catalyst interface resistance (R_s) and capacitance (CPE) and the charge-transfer resistance (R_{ct}) at the electrolyte–electrode interface. By measuring the fitted semicircles, $Co_{0.45}Fe_{0.55}PS_3$ possesses the smallest R_{ct} of 19 Ω, revealing excellent charge transfer efficiency. The corresponding overpotentials, Tafel slopes, and charge transfer resistances for all the $Co_xFe_{1-x}PS_3$ catalysts are listed in Table S1 (Supporting Information). Long-term stability is an essential factor for deciding electrocatalytic performance. The chronoamperometry was conducted to evaluate the potential at 1.55 V versus RHE during the long-term measurement. $Co_{0.45}Fe_{0.55}PS_3$ exhibits long-term stability of 20 h, indicating its potential for OER application under an alkaline environment (Figure 2d).

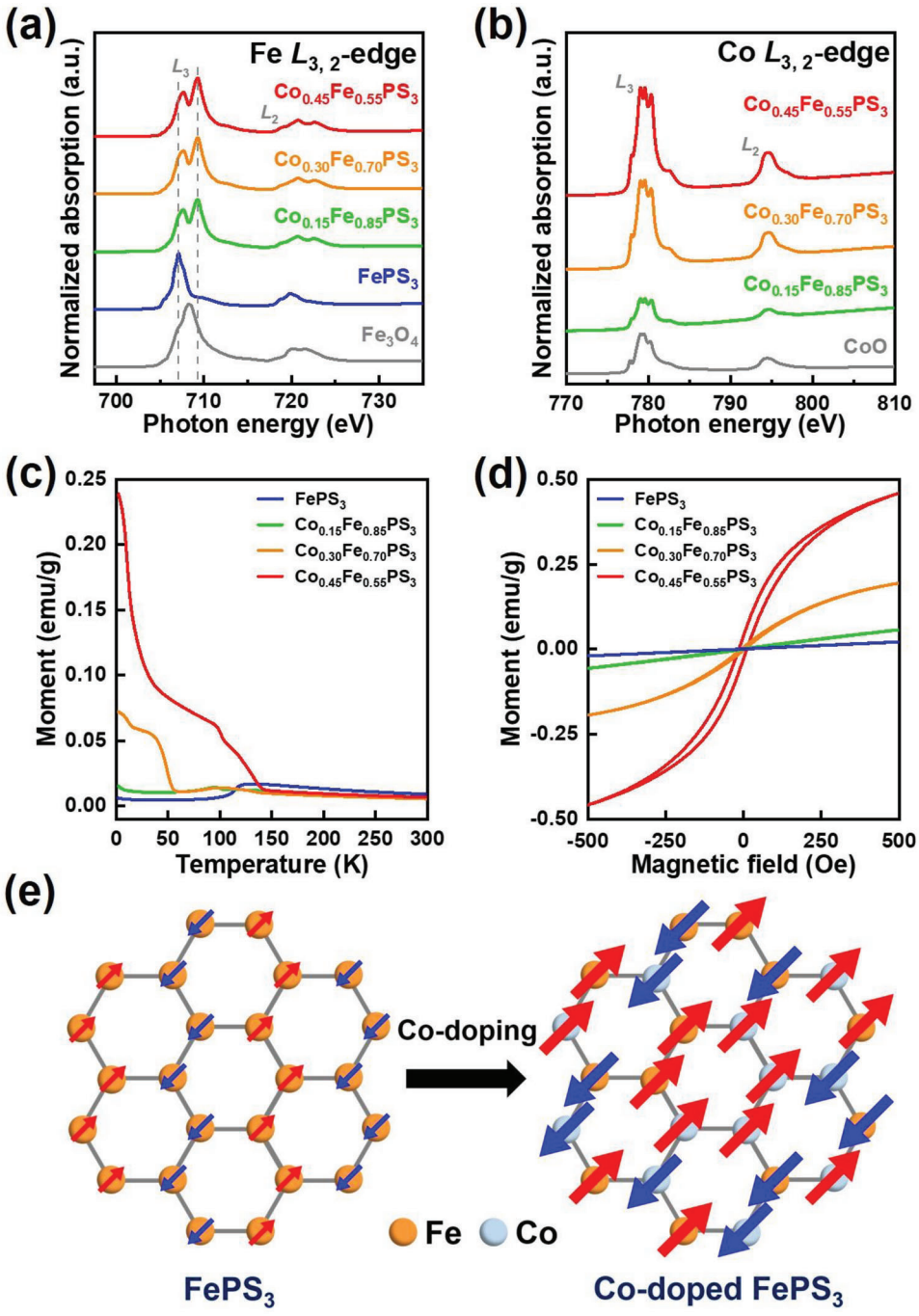

Figure 3. Electronic structures and magnetic properties of $Co_xFe_{1-x}PS_3$ crystals. a) Fe $L_{3,2}$-edge XANES spectra, and b) Co $L_{3,2}$-edge XANES spectra of various $Co_xFe_{1-x}PS_3$ together with Fe_3O_4 and CoO. c) Temperature dependence of the zero-field-cooled magnetization was measured at 100 Oe on various $Co_xFe_{1-x}PS_3$. d) Hysteresis loops measured at 5 K of $Co_xFe_{1-x}PS_3$. e) The illustration of magnetic moment distribution in the hexagonal lattice of $FePS_3$ and Co-doped $FePS_3$.

XANES was carried out at the TPS45A2 of the National Synchrotron Radiation Research Center (NSRRC), Taiwan to understand the electronic structures of $FePS_3$ and $Co_xFe_{1-x}PS_3$ (x = 0.15, 0.30, 0.45) crystals. **Figure 3**a,b displays the normalized Fe and Co $L_{3,2}$-edges XANES spectra of $FePS_3$ and $Co_xFe_{1-x}PS_3$ crystals, respectively. The reference Fe_3O_4, and CoO were obtained in the total electron yield mode, which primarily reveals the transition of electrons from Fe/Co $2p_{3/2}$ (L_3) and $2p_{1/2}$ (L_2) states to unoccupied Fe/Co $3d$ states. From Figure 3a, the line shapes of the Fe $L_{3,2}$-edge XANES spectra of $Co_xFe_{1-x}PS_3$ crystals are different from the pristine $FePS_3$ crystal, implying that Co doping can cause significant changes the electronic structures of Fe

3*d*-orbital in $Co_xFe_{1-x}PS_3$ crystals. The intensity of the Fe $L_{3,2}$-edges XANES spectra of $Co_xFe_{1-x}PS_3$ crystals gradually decreases as the Co doping concentration increases, which reflects a reduction in the number of unoccupied Fe 3d-derived states (Figure S2a, Supporting Information). Meanwhile, the general energy features of Co-doped $FePS_3$ crystals are close to those of the reference Fe_3O_4, indicating that Fe ions exist in the valence state of mixed Fe^{2+} and Fe^{3+} in all $Co_xFe_{1-x}PS_3$ crystals. The spectra exhibit a multipeak structure with two prominent features at ≈707.7 and 709.3 eV corresponding to Fe^{2+} and Fe^{3+} in the octahedral site.[23] By contrast, the pristine $FePS_3$ crystal only exhibits the Fe^{2+} peak, consistent with previous studies.[24] The presence of mixed valence Fe^{2+} and Fe^{3+} in $Co_xFe_{1-x}PS_3$ crystals may result from creating surface defects or vacancies during doping, where cobalt dopants break the symmetry in the crystalline structure of $FePS_3$.[25] In addition, the mixed-valence transition metals (Fe^{2+}/Fe^{3+}) have been reported to be beneficial to improving conductivity due to the electronic delocalization.[26] On the other hand, the line shapes and energy positions of the Co $L_{3,2}$-edges XANES spectra of $Co_xFe_{1-x}PS_3$ crystals are similar to those of reference CoO as shown in Figure 3b, inferring that the valence state of Co ions is 2+ charge in all $Co_xFe_{1-x}PS_3$ crystals. Cobalt 2+ ions are considered to possess a high-spin state ($t_{2g}^5e_g^2$) if they can be stabilized under octahedral sites.[27] The intensity of the Co $L_{3,2}$-edges XANES spectra of $Co_xFe_{1-x}PS_3$ crystals gradually increases as the Co doping concentration increases (Figure S2b, Supporting Information). It has been reported that the high-spin state Co^{2+} ($t_{2g}^5e_g^2$) cations in *d* orbital consisting of three unpaired electrons may ease the formation of a σ bond between OH^- adsorbate and Co atom, resulting in an enhanced OER performance.[13a] However, it is found that the pristine $CoPS_3$ shows a relatively poor electrocatalytic performance than the $Co_{0.45}Fe_{0.55}PS_3$, although $CoPS_3$ consists of a higher concentration of high-spin state Co^{2+} cations. (Figure S3, Supporting Information). The result implies that the origin of the enhanced catalytic activity of $Co_xFe_{1-x}PS_3$ depends not only on the concentration of cobalt dopants but also on other possible factors with the involvement of both Fe and Co ions.

Recently, Gracia and co-workers have proposed the theory of QSEI to explain the observed enhanced OER performance of magnetic-related catalysts.[9] Because the number of unpaired electrons is not conserved during OER, the spin potential in magnetic-related catalysts may act as a selective gate to affect the transport of local spin currents. The catalysts with AFM spin coupling exhibit much poorer conductivity and OER catalytic activity than those with FM coupling.[28] Here, we measured the static (dc) magnetic susceptibilities (χ = M/H) and magnetization for powder samples using a SQUID magnetometer to understand the magnetic properties of $FePS_3$ and $Co_xFe_{1-x}PS_3$ crystals. Figure 3c shows the temperature dependence of dc magnetic susceptibilities for $Co_xFe_{1-x}PS_3$ (x = 0, 0.15, 0.30, 0.45) in an applied field of μ_0H = 100 Oe with a temperature range of 2–300 K. All samples obey the Curie–Weiss law [$\chi(T) \approx C/(T-\theta)$] at high temperature ($T$ > 150 K), where χ is magnetic susceptibility, C is the Curie constant, and θ is referred to as the Curie–Weiss temperature. The AFM behavior is observed below the Néel temperature (T_N) ≈ 119 K for the pristine $FePS_3$, consistent with the literature.[29] As the Co concentration increases, these curves exhibit an AFM to FM transition in the $Co_xFe_{1-x}PS_3$ crystals with an increased x content. Figure 3d shows the field dependence magnetization for $Co_xFe_{1-x}PS_3$ (x = 0, 0.15, 0.30, 0.45) in the field range of −500 to 500 Oe at low temperature (5 K), which reveals that the FM interaction is getting stronger with increasing Co concentrations. The presence of Co is responsible for the suppression of long-range AFM correlations and the emergence of weak interatomic FM, resulting from the doping-mediated magnetic exchange interactions. Figure S4 (Supporting Information) shows the field dependence magnetization of $Co_{0.45}Fe_{0.55}PS_3$ measured at different temperatures, and results indicate that stronger FM interactions are developed with decreasing temperatures. The AFM interaction of pristine $FePS_3$ is predominantly resulting from strong third nearest-neighbors (TNN) exchange interaction (J_3) by forming a zig-zag pattern with alternating chains of antialigned Fe atoms, mediated by two S atoms located on the same chalcogen sublayer (Figure S5, Supporting Information).[30] This mechanism is known as superexchange interaction.[31] The presence of Co in $FePS_3$ could change the lattice configurations locally and disrupt the effective long-range hopping between two antiferromagnetically aligned TNN, inducing spin fluctuations in the system (Figure 3e) As a result, Co doping in the $Co_xFe_{1-x}PS_3$ crystals could induce ferromagnetism, which is predominated by the interactions from the first and the second nearest Fe neighbors (J_1 and J_2), where J_1 is stronger than J_2 (Figure S5, Supporting Information). A similar AFM to FM transition has been observed in the recent report on the defect-mediated $NiCoPS_3$ system, where the presence of sulfur vacancies in the $Ni_xCo_{1-x}PS_3$ may be responsible for the suppression of long-range AFM correlation and the emergence of weak FM interaction.[32] It is also believed that the addition of Co atoms in the $FePS_3$ crystal by doping may also create sulfur vacancies in the $Co_xFe_{1-x}PS_3$ crystals.[25b]

Figure 4a,b exhibits the spin-related partial density of states (pDOS) of $FePS_3$ and Co-doped $FePS_3$ calculated by density functional theory (DFT) simulations. The calculation details are described in the Supporting Information. The $FePS_3$ shows a symmetric spin-related pDOS with a large bandgap, where the net spin value of $FePS_3$ is zero. On the other hand, the Co-doped $FePS_3$ exhibits an asymmetry pDOS with a small bandgap, where the net spin value of Co-doped $FePS_3$ is not zero. According to QSEI, the predominant interatomic AFM orbital orderings leads to electronic localization, where the spins of neighboring magnetic centers mostly point in opposite directions. By contrast, the partial orbital filling of the FM covalent bonds allows the spin of the magnetic metals to point in the same direction. It was reported that such a phenomenon still prevails in catalysts even above the Curie temperature, where fast electronic transitions may occur through the locally available FM spin delocalization, even in the presence of oscillations due to vibrations and/or disordered magnetic domains.[9] Although the FM interaction of Co-doped $FePS_3$ is only observed at low temperatures according to the above magnetic measurement data in Figure 3d, the local unpaired spin configuration can be observed at room temperature. Figure S6 (Supporting Information) exhibits electron paramagnetic resonance (EPR) spectra of the $FePS_3$ and $Co_{0.45}Fe_{0.55}PS_3$ crystals under room temperature. There is no EPR signal for the pristine $FePS_3$, while the presence of a significant EPR signal from $Co_{0.45}Fe_{0.55}PS_3$ indicates a large number of unpaired

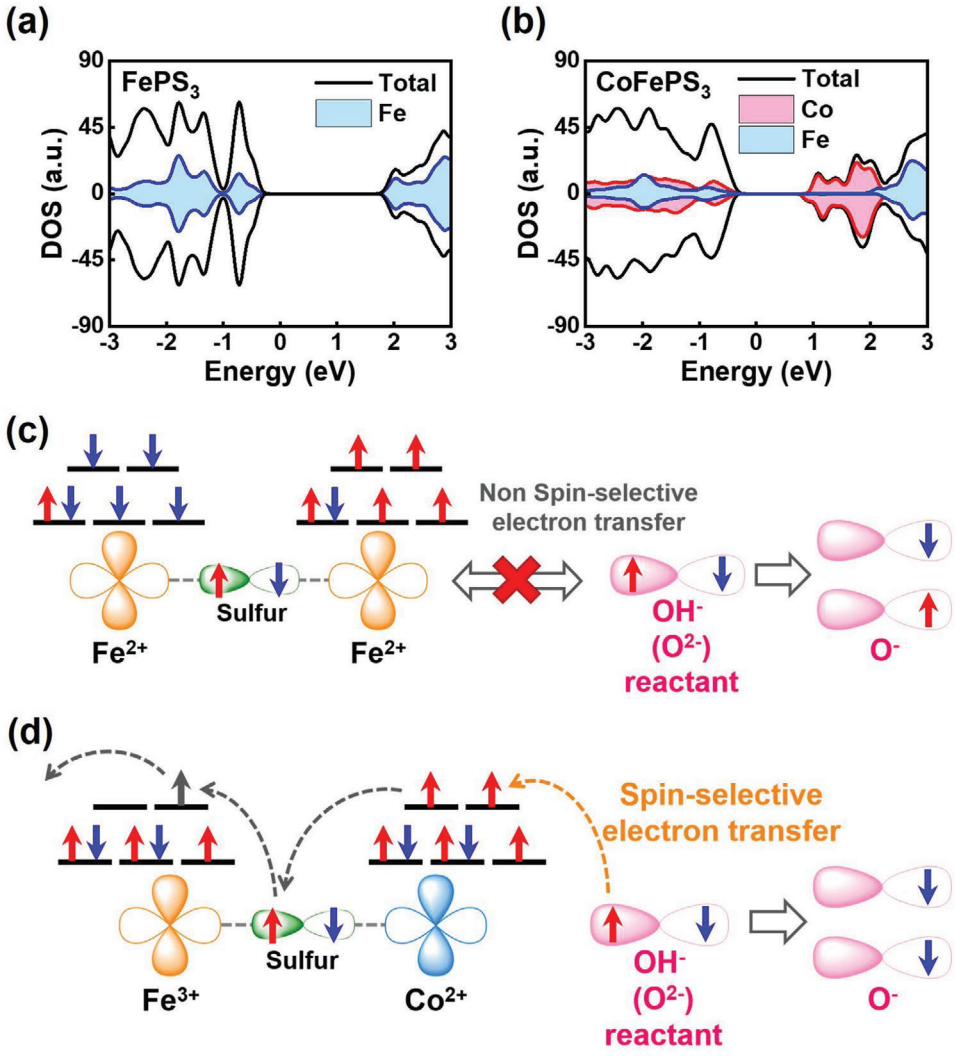

Figure 4. Density of state and spin-exchange interaction for OER. a) pDOS of $FePS_3$ and b) Co-doped $FePS_3$. The Fermi level is set to zero energy. c) Schematic illustration of the spin-selective channel in $FePS_3$ and d) Co-doped $FePS_3$.

electrons after Co doping. Therefore, more efficient spin-selected electron transport may occur at Co-doped $FePS_3$ as compared to the pristine $FePS_3$, according to QSEI. Figure 4c,d depicts the corresponding spin-related electron transfer mechanism of $FePS_3$ and Co-doped $FePS_3$, respectively. The presence of spin-up and spin-down characters in the neighboring iron cations of the pristine $FePS_3$ limits the mobility of spin-related electron transfer, resulting in poor OER performance (Figure 4c). By contrast, Co-doped $FePS_3$ consists of the mixed valences of Fe^{2+} and Fe^{3+} as shown in the above XANES data, where the Fe^{3+} is typically considered a combination of mixed high-spin (HS) and low-spin (LS) Fe^{3+} ions.[33] However, because LS Fe^{3+} ions are the ones that can provide the spin channel for electron transfer based on the QSEI theory, we only show the LS configuration in the schematic representation of Figure 4d. The coexistence of Fe^{3+} and Co^{2+} facilitated the spin-selective electron transfer process through the sulfur ions. The initial electron transfer step occurs through a spin-selective channel, resulting in the formation of an intermediate with a fixed spin direction, for example, $O^{-}(\downarrow)$. Subsequently, this intermediate can form the triplet state intermediate $O(\downarrow)O(\downarrow)H$, which leads to highly efficient OER performance (Figure 4d). From the above result, it is known that such a doping-mediated spin-selective electron transfer is essential for efficient OER. The high-spin state Co^{2+} cations ($t_{2g}^{5}e_g^{2}$) can selectively remove spin-oriented electrons from the reactants and facilitate the generation of triplet oxygen, enhancing the OER performance.[13a] Because $CoPS_3$ has a similar crystal structure to $FePS_3$, its spin-related electron transfer efficiency is low, owing to the e_g state of the Co^{2+} ions, which is not completely empty as likely Fe^{3+} ions. Therefore, $CoPS_3$ exhibits a relatively poor electrocatalytic performance than $Co_{0.45}Fe_{0.55}PS_3$, although $CoPS_3$ consists of a higher concentration of high-spin state Co^{2+} cations. Through doping the high-spin Co^{2+} in $FePS_3$, the synergistic effect of increasing the number of active sites and promoting spin-selected electron transfer boosts the overall OER catalytic activities of 2D $Co_xFe_{1-x}PS_3$ crystals. The complete spin-related OER mechanism is depicted in the supporting information of Figure S7 (Supporting Information).

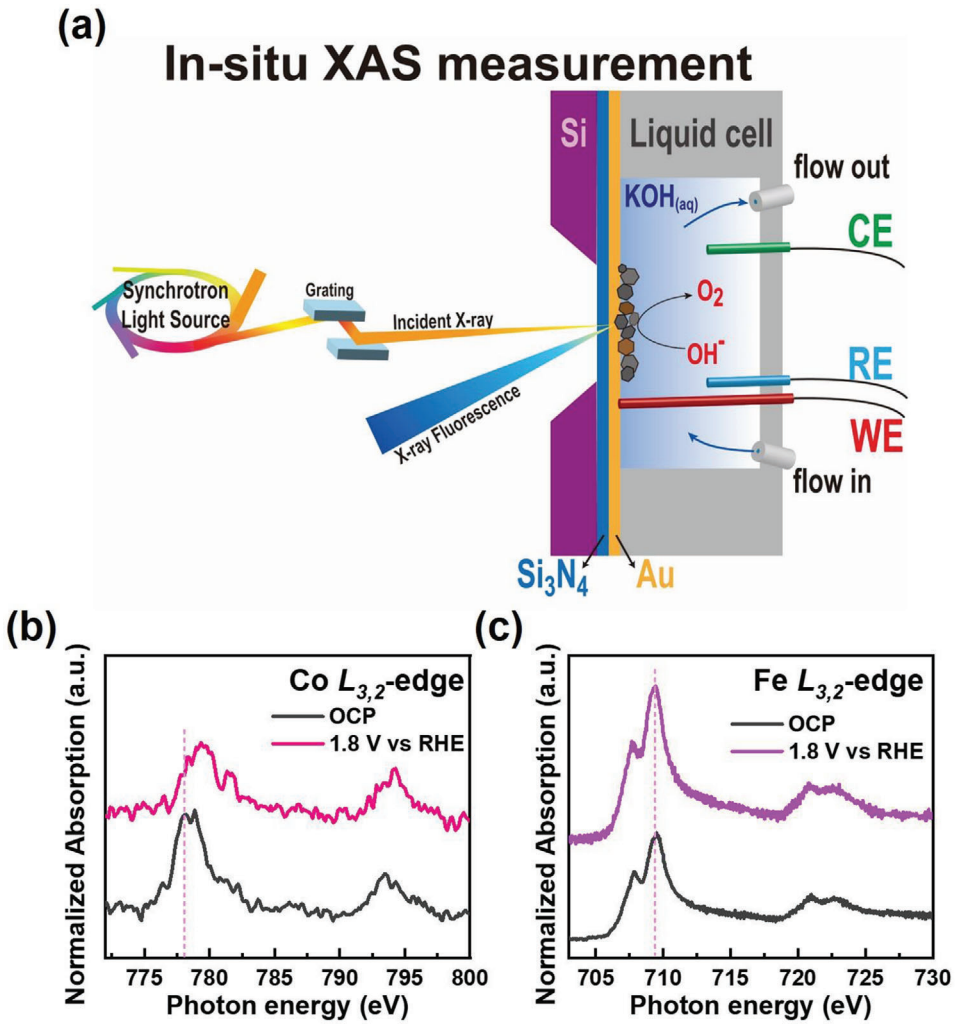

Figure 5. In situ XANES spectra. a) Illustration of in situ XANES setup. A liquid cell assembly includes valves for electrolyte flow in and out, a working electrode (WE) contacts with Si_3N_4 membrane, a counter electrode (CE), and a reference electrode (RE). b) Co and c) Fe $L_{3,2}$-edge XANES spectra of $Co_{0.45}Fe_{0.55}PS_3$ at OCP and applied 1.8 V versus RHE for the OER process.

To further support the enhanced spin-selective charge transfer of 2D $Co_xFe_{1-x}PS_3$ catalysts by doping, we performed in situ Co and Fe $L_{3,2}$-edge XANES measurements of $Co_{0.45}Fe_{0.55}PS_3$ in real-time during OER. The in situ soft X-ray experiment was also operated under an ultrahigh vacuum with a liquid cell at the TPS45A2 of NSRRC. **Figure 5**a shows the schematic illustration of the in situ XANES setup. The transition *d*-block metals are typically crucial in electrocatalysis owing to the unoccupied *d*-orbitals. The spectra of Co/Fe $L_{3,2}$-edge XANES are attributed to the transitions from Co/Fe 2*p* to 3*d* unoccupied orbitals, which can be utilized to observe the charge transfer behavior and oxidation state between the catalyst and reactant during the OER reaction. Figure 5b,c displays the in situ Co/Fe $L_{3,2}$-edge XANES of $Co_{0.45}Fe_{0.55}PS_3$ under open circuit potential (OCP), where no OER reaction occurs, and at 1.8 V versus RHE, where OER reaction occurs. The Co $L_{3,2}$-edge XANES spectra in Figure 5b shows a shift in the energy of L_3 absorption from 778.2 to 779.3 eV as the applied bias is changed from OCP to 1.8 V versus RHE. The result indicates that the oxidation state of Co in $Co_{0.45}Fe_{0.55}PS_3$ was changed from Co^{2+} close to Co^{3+} during OER, which means the intermediate species of Co(III)OOH was attached to Co sites.[34] Furthermore, the corresponding intensity of Co $L_{3,2}$-edge XANES decreases with an applied bias of 1.8 V compared to that at OCP, suggesting that cobalt atoms accept the electrons from the reactants, OH^-, to fill the unoccupied states at 3*d* orbitals of Co during the OER process.[12b,35] By contrast, there is no energy shift in the Fe $L_{3,2}$-edge XANES during OER, while the intensity of Fe $L_{3,2}$ absorption is slightly enhanced as the applied bias is changed from OCP to 1.8 V versus RHE (Figure 5c). The increased intensity of unoccupied states at 3*d* orbitals in the Fe $L_{3,2}$-edge XANES indicates some electrons transfer away from Fe ions and move to the other electrode for the counter-reaction of HER. The result indicates that Fe ions mainly play a role in the spin-selective charge transfer, not the oxidation process like Co ions. We also performed a similar experiment for the pristine $FePS_3$. The change in Fe $L_{3,2}$-edge XANES spectra of the pristine $FePS_3$ during OER under the same operation condition is almost negligible (Figure S8, Supporting Information), indicating no charge transfer occurs. The above Co and

Fe $L_{3,2}$-edge spectra of $Co_{0.45}Fe_{0.55}PS_3$ obtained from the in situ XANES experiment during the OER reaction suggests the efficient charge transfer process in $Co_{0.45}Fe_{0.55}PS_3$ is responsible for the outperformed OER catalytic activity compared to the pristine $FePS_3$, which also supports the above-proposed mechanism of in Figure 4c,d.

3. Conclusion

In summary, this work demonstrates the manipulation of spin-exchange interactions to enhance the spin-selected electron transfer efficiencies of 2D $Co_xFe_{1-x}PS_3$ ($x = 0$–0.45) vdW single crystals during OER reaction through Co doping. The presence of Co dopants in 2D $Co_xFe_{1-x}PS_3$ disrupts the antiferromagnetically aligned spin interactions of $FePS_3$ and causes the emergence of weak interatomic FM orbital ordering. Such doping-mediated magnetic exchange interaction is found to be responsible for the efficient spin-selected electron transfer between Co^{2+} and Fe^{3+}, leading to an efficient OER catalytic performance. The result is further evident from the SQUID magnetometer, in situ XANES analyses, and DFT simulations. Further exploration of those catalysts consisting of transition-metal elements by considering their spin configurations and spin-catalyzed reactions is particularly important for the future design of highly efficient OER catalysts.

Supporting Information

Supporting Information is available from the Wiley Online Library or from the author.

Acknowledgements

C.-W.C. acknowledges financial support from the National Science and Technology Council (NSTC) of Taiwan (Project No. 109-2124-M-002-002-MY3 and 109-2112-M-002-029-MY3). Financial support from the Center of Atomic Initiative for New Materials (AI-Mat), National Taiwan University, from the Featured Areas Research Center Program within the framework of the Higher Education Sprout Project by the Ministry of Education in Taiwan (Project No. 108L9008), is also acknowledged. R.S. acknowledges financial support from the NSTC of Taiwan under projects No. NSTC 111-2124-M-001-009 and NSTC 110-2112-M-001-065-MY3. W.-F.P. thanks the NSTC of Taiwan for providing financial support for research under the projects NSTC 112-2112-M-032-014 and NSTC 112-2112-M-032-009-MY2. J.-W.C. expresses gratitude to the NSTC of Taiwan for providing financial support for research under the projects NSTC 111-2112-M-390-003. The XANES spectra obtained from Taiwan Photon Source (TPS) 45A2 beamline at the National Synchrotron Radiation Research Center (NSRRC) are appreciated.

Conflict of Interest

The authors declare no conflict of interest.

Data Availability Statement

The data that support the findings of this study are available from the corresponding author upon reasonable request.

Keywords

electrocatalysis, in situ XANES, oxygen evolution reaction, spin catalysts, spin exchange interactions, van der Waals materials

Received: May 24, 2023
Revised: August 1, 2023
Published online:

[1] a) S. Chu, A. Majumdar, *Nature* **2012**, *488*, 294; b) T. R. Karl, K. E. Trenberth, *Science* **2003**, *302*, 1719.
[2] J. A. Turner, *Science* **2004**, *305*, 972.
[3] a) Z. Wang, C. Li, K. Domen, *Chem. Soc. Rev.* **2019**, *48*, 2109; b) Z. W. Seh, J. Kibsgaard, C. F. Dickens, I. Chorkendorff, J. K. Nørskov, T. F. Jaramillo, *Science* **2017**, *355*, eaad4998; c) T. Yao, X. An, H. Han, J. Q. Chen, C. Li, *Adv. Energy Mater.* **2018**, *8*, 1800210.
[4] a) P. J. McHugh, A. D. Stergiou, M. D. Symes, *Adv. Energy Mater.* **2020**, *10*, 2002453; b) I. Roger, M. A. Shipman, M. D. Symes, *Nat. Rev. Chem.* **2017**, *1*, 0003; c) H. Dotan, A. Landman, S. W. Sheehan, K. D. Malviya, G. E. Shter, D. A. Grave, Z. Arzi, N. Yehudai, M. Halabi, N. Gal, N. Hadari, C. Cohen, A. Rothschild, G. S. Grader, *Nat. Energy* **2019**, *4*, 786.
[5] Y. Jiao, Y. Zheng, M. Jaroniec, S. Z. Qiao, *Chem. Soc. Rev.* **2015**, *44*, 2060.
[6] Y. Sun, S. Sun, H. Yang, S. Xi, J. Gracia, Z. J. Xu, *Adv. Mater.* **2020**, *32*, 2003297.
[7] J. Suntivich, K. J. May, H. A. Gasteiger, J. B. Goodenough, Y. Shao-Horn, *Science* **2011**, *334*, 1383.
[8] J. Gracia, *Phys. Chem. Chem. Phys.* **2017**, *19*, 20451.
[9] C. Biz, M. Fianchini, J. Gracia, *ACS Catal.* **2021**, *11*, 14249.
[10] a) W. Mtangi, V. Kiran, C. Fontanesi, R. Naaman, *J. Phys. Chem. Lett.* **2015**, *6*, 4916; b) W. Mtangi, F. Tassinari, K. Vankayala, A. Vargas Jentzsch, B. Adelizzi, A. R. A. Palmans, C. Fontanesi, E. W. Meijer, R. Naaman, *J. Am. Chem. Soc.* **2017**, *139*, 2794.
[11] a) R. R. Chen, Y. Sun, S. J. H. Ong, S. Xi, Y. Du, C. Liu, O. Lev, Z. J. Xu, *Adv. Mater.* **2020**, *32*, 1907976; b) J. Gracia, R. Sharpe, J. Munarriz, *J. Catal.* **2018**, *361*, 331.
[12] a) F. A. Garcés-Pineda, M. Blasco-Ahicart, D. Nieto-Castro, N. López, J. R. Galán-Mascarós, *Nat. Energy* **2019**, *4*, 519; b) X. Ren, T. Wu, Y. Sun, Y. Li, G. Xian, X. Liu, C. Shen, J. Gracia, H.-J. Gao, H. Yang, Z. J. Xu, *Nat. Commun.* **2021**, *12*, 2608.
[13] a) J.-Y. Zhang, Y. Yan, B. Mei, R. Qi, T. He, Z. Wang, W. Fang, S. Zaman, Y. Su, S. Ding, B. Y. Xia, *Energy Environ. Sci.* **2021**, *14*, 365; b) Y. Sun, X. Ren, S. Sun, Z. Liu, S. Xi, Z. J. Xu, *Angew. Chem., Int. Ed.* **2021**, *60*, 14536; c) G. Shen, R. Zhang, L. Pan, F. Hou, Y. Zhao, Z. Shen, W. Mi, C. Shi, Q. Wang, X. Zhang, J.-J. Zou, *Angew. Chem., Int. Ed.* **2020**, *59*, 2313.
[14] a) X. Zhang, Y. Zhang, H. Yu, H. Zhao, Z. Cao, Z. Zhang, Y. Zhang, *Adv. Mater.* **2023**, 2207966; b) D. Ouyang, N. Zhang, Y. Li, T. Zhai, *Adv. Funct. Mater.* **2023**, *33*, 2208321.
[15] Q. H. Wang, A. Bedoya-Pinto, M. Blei, A. H. Dismukes, A. Hamo, S. Jenkins, M. Koperski, Y. Liu, Q.-C. Sun, E. J. Telford, H. H. Kim, M. Augustin, U. Vool, J.-X. Yin, L. H. Li, A. Falin, C. R. Dean, F. Casanova, R. F. L. Evans, M. Chshiev, A. Mishchenko, C. Petrovic, R. He, L. Zhao, A. W. Tsen, B. D. Gerardot, M. Brotons-Gisbert, Z. Guguchia, X. Roy, S. Tongay, et al., *ACS Nano* **2022**, *16*, 6960.
[16] F. Wang, T. A. Shifa, P. Yu, P. He, Y. Liu, F. Wang, Z. Wang, X. Zhan, X. Lou, F. Xia, J. He, *Adv. Funct. Mater.* **2018**, *28*, 1802151.
[17] a) Q. Liang, L. Zhong, C. Du, Y. Luo, J. Zhao, Y. Zheng, J. Xu, J. Ma, C. Liu, S. Li, Q. Yan, *ACS Nano* **2019**, *13*, 7975; b) J. Zhang, N. Zhou, M. Du, Y. Li, Y. Cui, X. a. Li, X. Zhu, W. Huang, *J. Mater. Chem. A* **2022**, *10*, 296.
[18] a) S. Xue, L. Chen, Z. Liu, H.-M. Cheng, W. Ren, *ACS Nano* **2018**, *12*, 5297; b) W. Zhu, W. Gan, Z. Muhammad, C. Wang, C. Wu, H. Liu, D. Liu, K. Zhang, Q. He, H. Jiang, X. Zheng, Z. Sun, S. Chen, L. Song, *ChemComm* **2018**, *54*, 4481; c) Q. Liang, L. Zhong, C. Du, Y. Luo, Y. Zheng, S. Li, Q. Yan, *Nano Energy* **2018**, *47*, 257.

[19] B. Song, K. Li, Y. Yin, T. Wu, L. Dang, M. Cabán-Acevedo, J. Han, T. Gao, X. Wang, Z. Zhang, J. R. Schmidt, P. Xu, S. Jin, *ACS Catal.* **2017**, *7*, 8549.
[20] F. M. Oliveira, J. Paštika, V. Mazánek, M. Melle-Franco, Z. Sofer, R. Gusmão, *ACS Appl. Mater. Interfaces* **2021**, *13*, 23638.
[21] a) B. Dong, M.-X. Li, Y.-N. Zhou, R.-Y. Fan, Y.-M. Chai, *Int. J. Hydrogen Energy* **2022**, *47*, 27508; b) Z. Wang, S. Shen, Z. Lin, W. Tao, Q. Zhang, F. Meng, L. Gu, W. Zhong, *Adv. Funct. Mater.* **2022**, *32*, 2112832.
[22] B. L. Ellis, W. R. M. Makahnouk, W. N. Rowan-Weetaluktuk, D. H. Ryan, L. F. Nazar, *Chem. Mater.* **2010**, *22*, 1059.
[23] a) A. Mirone, M. Sacchi, S. Gota, *Phys. Rev. B* **2000**, *61*, 13540; b) B. Y. Wang, H. T. Wang, S. B. Singh, Y. C. Shao, Y. F. Wang, C. H. Chuang, P. H. Yeh, J. W. Chiou, C. W. Pao, H. M. Tsai, H. J. Lin, J. F. Lee, C. Y. Tsai, W. F. Hsieh, M. H. Tsai, W. F. Pong, *RSC Adv.* **2013**, *3*, 7884.
[24] A. G. Chang, L.-W. Lan, Y.-J. Chan, C.-N. Kuo, T. Chen, C.-H. Huang, T.-H. Chuang, D.-H. Wei, C.-S. Lue, C.-C. Kuo, *Phys. Rev. B* **2022**, *106*, 125412.
[25] a) Z. Yu, J. Peng, Y. Liu, W. Liu, H. Liu, Y. Guo, *J. Mater. Chem. A* **2019**, *7*, 13928; b) A. Dhanarajgopal, P.-C. Chang, S.-Y. Liu, T.-H. Chuang, D.-H. Wei, C.-C. Kuo, C.-N. Kuo, C. S. Lue, W.-C. Lin, *Appl. Surf. Sci.* **2021**, *567*, 150864.
[26] L. S. Xie, L. Sun, R. Wan, S. S. Park, J. A. DeGayner, C. H. Hendon, M. Dincă, *J. Am. Chem. Soc.* **2018**, *140*, 7411.
[27] H. Wu, T. Burnus, Z. Hu, C. Martin, A. Maignan, J. C. Cezar, A. Tanaka, N. B. Brookes, D. I. Khomskii, L. H. Tjeng, *Phys. Rev. Lett.* **2009**, *102*, 026404.
[28] a) R. Sharpe, T. Lim, Y. Jiao, J. W. Niemantsverdriet, J. Gracia, *ChemCatChem* **2016**, *8*, 3762; b) L. Zhang, A. Cheruvathur, C. Biz, M. Fianchini, J. Gracia, *Phys. Chem. Chem. Phys.* **2019**, *21*, 2977.
[29] J.-U. Lee, S. Lee, J. H. Ryoo, S. Kang, T. Y. Kim, P. Kim, C.-H. Park, J.-G. Park, H. Cheong, *Nano Lett.* **2016**, *16*, 7433.
[30] B. L. Chittari, Y. Park, D. Lee, M. Han, A. H. MacDonald, E. Hwang, J. Jung, *Phys. Rev. B* **2016**, *94*, 184428.
[31] P. W. Anderson, *Theory of Magnetic Exchange Interactions: Exchange in Insulators and Semiconductors*, Academic Press, Cambridge, **1963**.
[32] F. Wang, N. Mathur, A. N. Janes, H. Sheng, P. He, X. Zheng, P. Yu, A. J. DeRuiter, J. R. Schmidt, J. He, S. Jin, *Sci. Adv.* **2021**, *7*, eabj4086.
[33] J.-F. Lin, S. Speziale, Z. Mao, H. Marquardt, *Rev. Geophys.* **2013**, *51*, 244.
[34] a) J. Okamoto, H. Nakao, Y. Yamasaki, H. Wadati, A. Tanaka, M. Kubota, K. Horigane, Y. Murakami, K. Yamada, *J. Phys. Soc. Jpn.* **2014**, *83*, 044705; b) T.-H. Lu, C.-J. Chen, Y.-R. Lu, C.-L. Dong, R.-S. Liu, *J. Phys. Chem. C* **2016**, *120*, 28093.
[35] T. Wu, X. Ren, Y. Sun, S. Sun, G. Xian, G. G. Scherer, A. C. Fisher, D. Mandler, J. W. Ager, A. Grimaud, J. Wang, C. Shen, H. Yang, J. Gracia, H.-J. Gao, Z. J. Xu, *Nat. Commun.* **2021**, *12*, 3634.